

Improved materials characterisation through the application of geometry reconstruction to quasi-static and high strain rate tension tests.

MR Arthington, CR Siviour, N Petrinic

Dept. Engineering Science, University of Oxford, Oxford, OX1 3PJ, UK

Abstract

This paper presents novel materials characterisation techniques for expanding the range of data obtained from tensile tests at quasi-static and high strain rates. Through the application of photography and a geometry reconstruction technique, we obtain data for Steel and Zirconium, with an emphasis on the new opportunities afforded by these techniques. The paper extends the state of the art in tensile characterisation, improving the range of data that can be obtained, and is supported by a number of validation measurements. In particular, calculations of cross-sectional area, shape and ellipticity are presented. These calculations can be performed as functions of both time and axial position. Therefore, it is possible to calculate mean true stress-strain relationships in the material, without the corrections that are required when such relationships are calculated simply using load and displacement data from the ends of the specimen. Steel and Zirconium were selected for their distinct degrees of anisotropy, giving a robust assessment of the capabilities of the techniques. In the future, such measurements will allow researchers to more closely measure, understand, and model, mechanical properties of materials over a wide range of strain rates.

Keywords: Hopkinson bar, high speed photography, geometry reconstruction, Zirconium, Steel

Email addresses: `matthew.arthington@eng.ox.ac.uk` (MR Arthington),
`clive.siviour@eng.ox.ac.uk` (CR Siviour), `nik.petrinic@eng.ox.ac.uk` (N Petrinic)

1. Introduction: High Strain Rate Tensile Testing

Since the pioneering work of Harding and colleagues [1, 2], the Tensile Split Hopkinson Bar [SHTB] has been one of the techniques used to characterise the mechanical response of materials to high strain rate deformation [3, 4, 5]. However, the data obtained from tensile tests are limited by the onset of necking. In particular, once necking has occurred, even if the material volume remains constant, true stress cannot be calculated accurately from the applied load and global deformation rate alone, as it can in compression experiments in which barrelling is prevented by careful specimen design and good lubrication [6].

Necking in tensile specimens is a result of a plastic instability in the specimen where the rate of increasing strength of the material through strain hardening is no longer sufficient to support the rate of increasing load. The weakest location along the gauge length of the specimen starts to narrow, which causes further concentration of the stress and further narrowing of that neck.

The curvature in the neck results in a triaxial stress state within the specimen which cannot be analysed by simply assuming a prismatic cross-section. Bridgman [7] suggested a correction factor to obtain the effective uniaxial stress from a necking isotropic specimen using the curvature of the neck:

$$\sigma_{eff} = \frac{\sigma_{avg}}{\left(1 + \frac{2R}{r}\right) \left[\ln\left(1 + \frac{r}{2R}\right)\right]} \quad (1)$$

where σ_{eff} is the effective stress that would be present if the gauge section were parallel, σ_{avg} is the total axial force divided by the cross-sectional area, r is the radius of the cross-section and R is the radius of the profile. Using this approximation a better estimate of the true stress during loading can be found for many materials.

The Bridgman correction relies on the cross-section remaining circular and the von Mises yielding criterion applying. Eisenberg [8] presented a modification of the Bridgman correction to include anisotropic materials with initially circular cross-sections that deform into ellipses. To calculate effective stress, the correction equation suggested was:

$$\sigma_{eff} = \frac{\sigma_{avg}}{\frac{1}{2} + \frac{1}{4} \left(1 + \frac{R_a}{r_a}\right) \ln\left[1 + \frac{r_a}{R_a}\right] + \frac{1}{4} \left(1 + \frac{R_b}{r_b}\right) \ln\left[1 + \frac{r_b}{R_b}\right]} \quad (2)$$

where r_a and r_b are the lengths of the semi-major and semi-minor axes respectively at the minimum cross-sectional area, and R_a and R_b are the profile radii corresponding to the major and minor axes of the ellipse. When equation 2 is valid, the correction from σ_{avg} to σ_{eff} can be made for any elliptical cross-sections when measurements are made of the specimen geometry.

In order to obtain the radius of curvature, an independent measurement of the radius of the specimen as a function of axial position may be made using high speed photography, (e.g. [9]). For initially cylindrical specimens of isotropic materials, which retain their circular cross-section throughout the experiment, photographs from a single angle are sufficient. However, there are many materials for which this is not the case. The hcp metals (e.g. Titanium and its alloys, and Zirconium) have mechanical properties that are highly dependent on grain orientation, and if their production route leads to a preferred orientation, or texture, initially circular cross-sections will deform into ellipses [10, 11, 12].

The authors have recently developed a technique by which the elliptical cross-section of a specimen can be reconstructed from three photographs of the specimen from different angles [13]. The method is shown in figure 1, where it can be seen that three views of the specimen are used to obtain its profiles. These profiles are then used to calculate six lines, at all discernible axial positions, that are tangential to the specimen's surface. Five unique tangential lines would be sufficient to describe a general ellipse, and the six lines together are used in a least-squares technique to find the ellipse that minimises the distance to the lines at every position.

The reconstruction at distinct axial positions produces the five key parameters that define the ellipse: lengths of semi-major (r_a) and semi-minor (r_b) axes, orientation (ϕ) and also the x and y co-ordinates of the centre of the ellipse, these parameters are shown in figure 2. By repeating the photographs throughout the duration of the experiment, a deformation history can be constructed. Recent papers have described the reconstruction process in detail, [13], and also its application to Taylor Impact experiments on Zirconium [14].

The current paper focuses on extending the state of the art in high strain rate tensile tests by demonstrating how this technique can be used to derive important information on the deformation history of specimens, using clock-rolled commercially pure Zirconium (highly anisotropic) and Steel (isotropic) as model materials. From this history, a number of important material properties can be derived. In particular, the work presented in this paper con-

centrates on the following:

- Mean true direct stress as a function of true axial strain;
- Radial strains as a function of true axial strain;
- Anisotropy as a function of true strain, as defined by the R ratio, the ratio of transverse strains [15].

It is also shown that accurate curvature measurements can be made throughout the length of the specimen along major and minor cross-section axes. Data will be shown from quasi-static and Hopkinson bar experiments. Such measurements represent a significant improvement in the characterisation of these materials.

2. Specimens and Experimental set-up

Specimens were manufactured from two materials. One of these was a commercial Steel rod, which was expected to exhibit isotropic mechanical properties. The other was the same Zirconium plate used in the previous Taylor Impact experiments [14]; work is on-going to fully describe the characterisation of this plate at different strain rates in tension and compression. The parent material is a plate of clock-rolled commercially-pure Zirconium (CP-Zr) 6.35 mm thick. The rolling process causes the hcp grains to be orientated with the c-axis lying favourably, but randomly, in the through-thickness direction of the plate to produce a transversely isotropic microstructure. The mechanical properties of the plate are also expected to be transversely isotropic, but will be significantly different in the through thickness direction. The outcome for the experiments reported here is that, for tensile specimens cut from an in-plane direction, the radius that was in the plane of the plate deforms significantly more than the radius perpendicular to the plane of the plate, see figure 3. Thus the initially circular cross section evolves to an ellipse. Tensile specimens were cut from the plate and rod to the dimensions shown in figure 3.

Quasi-static experiments were performed using a commercial screw-driven device at a measured true total strain rate of $1.6 \times 10^{-3} s^{-1}$ for the Zirconium and $3.3 \times 10^{-3} s^{-1}$ for the Steel. Three cameras were arranged around the specimen, with an angle of 45° between them, and used to acquire images at a rate of one every three seconds. High rate experiments were performed using

a tensile split-Hopkinson bar with 10 mm diameter input and output rods of Titanium alloy (Ti-6Al-4V) and Phosphor Bronze respectively. The true plastic strain rate experienced in the neck of the specimen as it deformed was 4400 s^{-1} for the Zirconium and 5600 s^{-1} for the Steel. Photographs were acquired using a SIMX16 camera, manufactured by Specialised Imaging Limited, which produces 16 frames of a little over 1 MPixel resolution. The frame rate was c.a. 10^5 frames per second, and the exposure time was $2\text{ }\mu\text{s}$. In order to produce three images of the specimen at high rates, two mirrors were used: each frame from the camera contains three images, spaced at 60° . The experimental set-up and geometry at both quasi-static and high strain rates are identical to that described in [13], which also contains an assessment of the accuracy and potential sources of error in the methodology, except that the illumination set-up was modified so that all pictures of the specimens were silhouettes, which aids the edge detection process.

A schematic diagram of the tensile split-Hopkinson bar system is shown in figure 4. This consists of a long loading bar, with a flange at one end, which is impacted by a gas gun driven tube to produce a tensile stress wave. The wave propagates down the loading bar to the input bar. This Titanium alloy (Ti64) input bar is 10 mm in diameter, 500 mm long and is instrumented with two sets of strain gauges. The specimen sits between the input bar and a Phosphor Bronze output bar, of the same dimensions and instrumented with one set of strain gauges. The force and velocity of the input bar-specimen interface is calculated from the two strain gauge signals using a wave separation method outlined in [2]. The force and velocity of the specimen-output bar interface is calculated from the strain gauge signal. By using a low-wavespeed Phosphor Bronze output bar and two gauges on the input bar, the duration of the experiment is extended beyond that which would be possible with a single gauge on the input bar. Because of the small input and transmitted bar diameters, and long loading bar, dispersion corrections are not required between the gauges and the specimen-bar interfaces.

Once the two sets of force-time and velocity-time profiles have been calculated, for the two ends of the specimen, these can be used to calculate stress-strain relationships in the specimen. The two forces are compared to establish that the specimen is in a state of stress equilibrium, although only output bar forces are reported. The two velocities are used to calculate the deformation rate, and thus the strain in the specimen. Early in the experiment, the analysis procedure must take into account the fact that the input bar begins moving *before* the stress wave reaches the output bar.

This means that an apparent strain is calculated before the stress at the output bar interface begins to rise, and some means of correcting for this must be adopted. Further time-shifting of the pulses requires knowledge, or assumptions, about the specimen behaviour, but the high speed photographs provide an opportunity to correct the data for this effect *and* for strains that accumulate outside the gauge length of the specimen.

In order to demonstrate this, and to provide a baseline measurement of material properties, nominal stress-strain curves are provided in figure 5. The quasi-static curves were calculated using the force from the load cell and displacement data from Digital Image Correlation tracking of the specimen shoulders. The high strain rate curves, figure 6, were calculated as described above. The strain calculated from the interface velocities produced the curve called ‘Initial SHP wave analysis strain’. Digital Image Correlation was used to track the motion of the specimen shoulders in the photographs taken during the experiment. 16 measurements were made, one for each frame from the camera, and the correlation was performed by comparison to a series of 16 static images taken before the experiment started. This produces a piecewise stress-strain curve labelled ‘DIC strain’. Using the 16 strain values, the strain produced from the interface velocities was then shifted and scaled to produce the curve ‘Shifted and scaled strain’.

3. Preliminary Data

3.1. Validation of Specimen Shape

In order to confirm that the cross-sections of the specimens did become elliptical during deformation, and did not take on some other shape, a specimen of each material was subjected to an interrupted quasi-static experiment, in which the loading was stopped and the specimens removed at a nominal strain of 23%. These specimens were measured using a Mitutoyo SERIES 191 CNC Coordinate Measurement Machine (CMM), which was used to record the positions of a large number of points around the circumference of the specimens at different positions along their axial length. Figure 7 shows images of the two specimens, and indicates two locations where the CMM data were gathered that were found to have the least agreement with their corresponding fitted ellipses, inside and outside of the gauge section.

Figure 8 shows the result of fitting ellipses to the CMM data, the radial ‘spikes’ indicate the distance between each CMM data point and the best fit ellipse. It should be noted that the length of these spikes has been scaled

to 20 times the scale in the x and y directions. There is a trade-off in the CMM between axial and radial accuracy; for the measurements in figure 8, the radial accuracy was optimised at the expense of axial position, as this is the best arrangement for the validation. These data give strong confirmation that an ellipse is the appropriate shape to describe the cross-sections of these specimens at all levels of deformation. Again, it should be noted that the data in figure 8 represent the *worst* case for both the Zirconium and the Steel specimens. The mean distance from the CMM data point values to the corresponding fitted ellipse provides a measure of the deviation of the cross-section from elliptical. These values were calculated at each cross-section throughout the gauge length for both specimens. For Zirconium, the mean distance from the fitted ellipses across the gauge length had a maximum value of $6.1\ \mu\text{m}$; a mean value of $2.2\ \mu\text{m}$ and a standard deviation of $1.1\ \mu\text{m}$. For Steel, the mean distance from the fitted ellipses across the gauge length had a maximum value of $1.7\ \mu\text{m}$; a mean value of $0.7\ \mu\text{m}$ and a standard deviation of $0.3\ \mu\text{m}$.

3.2. Validation of key parameters from optical reconstruction

Whilst the CMM data provide an excellent confirmation that the use of elliptical cross-sections is appropriate, they were not used to validate key data from the geometric reconstruction. This was because the CMM was unable to accurately register the axial position for specimens with this level of curvature without compromising the radial position measurements.

Instead, the geometry reconstruction, from photographs taken after the interrupted specimens had been unloaded, and just before they were removed from the load frame, was confirmed using an optical comparator (Mitutoyo Profile Projector PV-600) to measure diameters of the specimen at different axial positions. Measurements were made at two different orientations. The first orientation was chosen to minimise the diameter of the neck, to produce $2r_b$, the second orientation was at 90° and produced $2r_a$.

Figure 9 compares the *areas* of the specimens calculated from geometric reconstruction and the optical comparator, showing very good agreement between the two techniques. The percentage difference in calculated area throughout the gauge length for the Zirconium specimen had a greatest value of -1.27% , a mean of -0.75% and a standard deviation of 0.33% . The percentage difference in calculated area throughout the gauge length for the Steel specimen had a greatest value of -1.47% , a mean of -0.50% and a standard deviation of 0.30% .

Figure 10 compares the aspect ratios of the specimens, an important measure of the degree of ellipticity defined as

$$\text{aspect ratio} = \frac{r_a}{r_b} \quad (3)$$

It is noted that the, in principle isotropic, steel specimen does exhibit some ellipticity in its cross section at high strains. The percentage difference in aspect ratio throughout the gauge length for the Zirconium specimen had a greatest value of -0.98% , a mean of -0.14% and a standard deviation of 0.38% . The percentage difference in aspect ratio throughout the gauge length for the Steel specimen had a greatest value of 0.69% , a mean of 0.17% and a standard deviation of 0.21% .

One further use for the ellipses fitted to the CMM data was to confirm the observation from the geometry reconstruction that the *orientation* (ϕ) of the ellipses did not change along the specimen length; since orientation is therefore independent of axial position, the CMM errors do not affect the comparison, figure 11. It is noted that this validation cannot be performed using optical comparator data, since the method used to gather these data assumes the orientation of the ellipse. Validation data are only shown for the Zirconium specimen: because the cross-section of the steel specimens remained very close to circular, measurements of ϕ are meaningless.

4. Zirconium and Steel: Results and Discussion

4.1. Data obtained from reconstruction

Before the geometry reconstruction was performed, images were calibrated using the procedure described in [13]. Additionally, in order to move the data from the (static) camera frame of reference to the (moving) specimen frame of reference, the images were translated to axially align the position of the end of the specimens which moved least. In all cases this was done using Digital Image Correlation to align one corner of the specimen shoulder in all the frames.

The key output from the geometry reconstruction consists of the values of r_a , r_b and ϕ for every pixel along the specimen length for every set of three images. These values allow the area of the specimen to be calculated

$$A = \pi r_a r_b \quad (4)$$

and, in turn, the mean true direct stress as a function of axial position. It is useful to define the local true axial strain by assuming that the volume of the specimen does not change, i.e.

$$\varepsilon_A = \ln \left(\frac{A_0}{A} \right) \quad (5)$$

where A_0 is the initial specimen area and the subscript A indicates that the strain has been calculated from the area ratio. This strain is particularly useful as it is also defined at every pixel along the specimen length. Finally, we define the R ratio as

$$R = \frac{\ln(r_a/r_0)}{\ln(r_b/r_0)} \quad (6)$$

where r_0 is the initial radius of the specimen, i.e. the R ratio is the ratio of the true strains in the directions of the major and minor axes of the ellipse. This is a different definition to that used by Kocks [15] and the ASTM standard [16], where the ratio of strains in pre-defined material directions is used. The definition in equation 4 allows the principal strain directions to differ from the material directions, but also requires the orientation of the ellipse with respect to material axes to be quoted for all values of R.

Figure 12 shows the output data for r_a and r_b as functions of position and time. For reconstruction purposes a low-pass filter was used to remove noise from the high rate data, the effect of this filter is shown. These data clearly show the anisotropy of the Zirconium specimens, for which the radius in the semi-major axis changes very little with strain.

5. Calculation of material properties

A more useful representation of material behaviour is to plot relevant properties against strain. In order to do this for as large a strain as possible, relevant material properties were calculated for each image at the position of largest strain (i.e. smallest area). Before the neck forms, this may be anywhere on the gauge length; after the neck forms it is the centre of the necked region. Figure 13 shows the reconstructed shape of the specimen cross section at the position of largest strain as the experiments progressed. For the Zirconium specimen, the radius in the plane of the original plate decreased significantly, whilst the other radius only changed slightly. It is noted that the axes of the ellipse are not precisely aligned with the plate directions, and

that the orientation of the elliptical cross-section does not change with strain. The cross-section of the Steel specimen remains almost circular; however some ellipticity is observed and this will be further quantified below.

Figure 14 shows mean-true-direct-stress true-strain curves derived using the measurements of specimen area. Both specimens were taken to failure, and photographs were captured up to, and beyond, the moment of failure. The ultimate tensile strength (UTS), obtained from Nominal stress plots, is indicated. The curve for the quasi-static experiments is much smoother; approximately 150 photographs were taken during these experiments. Only 16 photographs were taken in the high rate experiments, of which 3 were after failure occurred; dots on the stress-strain curve indicate the location of those photographs taken during loading. The Zirconium exhibits an increase in strength and decrease in ductility under high rate loading, compared to quasi-static; the steel specimens show the increase in strength without the decrease in ductility. The similarity between the failure strains of the two materials is coincidental. In addition, these data allow the true strain rate experienced in the neck to be calculated. This was 4400 s^{-1} for Zirconium and 5600 s^{-1} for steel.

Figure 15 shows r_a and r_b as functions of strain, it is observed that the strain dependence of these radii is independent of strain rate. Figure 16 shows the R ratio, where $R = 1$ for a circle and $R = 0$ for a line. This measurement shows again that for the Zirconium, the R ratio is independent of strain rate, but increases slightly with increasing strain. For Steel, the measurement indicates firstly that the material is slightly anisotropic, and secondly that there is small rate dependence but no strain dependence. It should be noted that the R ratio is poorly defined before the UTS as the strains are very small, and the ratio is dominated by noise; for this reason data for very small strains are not shown.

In addition to measurements of specimen radius, radius of curvature is an often used measurement. For instance it is used in the Bridgman [7] correction and Eisenberg's modification [8] for estimating the effective stress in the three dimensional stress state at the neck. Figure 17 shows the radius and the curvature for Zirconium tested at quasi-static and high strain rates in the last frame captured before fracture. Here, 'curvature' is defined as the inverse of the radius of curvature, and is a more convenient measure in cases such as this when the radius of curvature frequently goes to infinity. Obtaining these data requires differentiation of the radii data, and therefore the data were smoothed first. For ease of evaluation, the following data

are presented for the major and minor radii: radius, smoothed radius and curvature. These data are presented to show that the techniques are robust enough to reliably calculate such properties.

To exemplify the use of such data in estimating the effective stress immediately before fracture in the Zirconium specimens the radii and curvatures at the neck are recorded: for the quasi-static specimen, $r_a = 1.36$, $r_b = 0.752$, curvature $1/R_a = 0.223$ and $1/R_b = 0.564$; and for the high strain rate specimen $r_a = 1.429$, $r_b = 0.964$, curvature $1/R_a = 0.131$ and $1/R_b = 0.429$. Now equation 2 is applied to give an effective stress of $\bar{\sigma} = 0.925\sigma$ and $\bar{\sigma} = 0.937\sigma$ for the quasi static and the high strain rate specimens respectively.

6. Conclusions

When specimens with initially circular cross-sections are deformed under uniaxial loading in tension, the cross section frequently becomes elliptical. By taking photographs of such specimens from three different angles, it is possible to calculate the parameters of the ellipses formed as functions of axial position and time, a process described here as geometric reconstruction. Of particular importance are the lengths of the semi-major and semi-minor axes, from these it is possible to calculate the R ratio, a description of the amount of ellipticity exhibited. Moreover, the data obtained can be used to calculate mean-true stress against true strain curves for the specimen material; in particular, it is possible to extend these calculations beyond neck formation until specimen failure. Finally, measurements of curvature of the specimen surface are presented, which have been used to exemplify the estimation of the effective stress.

The data obtained from Zirconium show that the elliptical cross section of the deformed specimen is approximately aligned with the directions of the parent plate material. The deformed material is highly elliptical, with an R ratio less than 0.1, although this value has some strain, but no strain rate, dependence. Conversely, the R ratio for the Steel, which was slightly anisotropic, exhibited a small strain rate, but no strain, dependence.

Acknowledgements

M.R. Arthington would like to thank EPSRC and Rolls-Royce plc (in particular J. Reed) for their sponsorship of his doctoral studies. The authors would like to thank R. Froud, R. Duffin and S. Carter for their skilled

manufacture of specimens and test apparatus used in these experiments. F. Hoffman assisted greatly in recording the CMM measurement data and we also thank P. Webb for making the accurate optical comparator measurements. Early experiments performed during this research made use of a SIM16 camera provided by the EPSRC Engineering Instrument Pool, and we are grateful for the assistance of A. Walker during this loan period.

References

- [1] J. Harding, E. Wood, J. Campbell, Tensile testing of materials at impact rates of strain., *J Mech Eng Sci* 2 (1962) 88–96.
- [2] J. Harding, L. Welsh, A tensile testing technique for fiber-reinforced composites at impact rates of strain, *Journal of Materials Science* 18:6 (1983) 1810–1826.
- [3] S. Nemat-Nasser, High strain rate tension and compression tests, *asm handbook* 8 (2000) 428–446.
- [4] G. Gray, Classic split-hopkinson pressure bar testing, *asm handbook* 8 (2000) 462:476.
- [5] J. E. Field, S. M. Walley, W. G. Proud, H. T. Goldrein, C. R. Siviour, Review of experimental techniques for high rate deformation and shock studies, *International Journal of Impact Engineering* 30 (2004) 725–775. Fifth International Symposium on Impact Engineering.
- [6] P. Li, C. Siviour, N. Petrinic, The effect of strain rate, specimen geometry and lubrication on responses of aluminium aa2024 in uniaxial compression experiments, *Experimental Mechanics* 49 (2009) 587–593. 10.1007/s11340-008-9129-1.
- [7] P. Bridgman, The stress distribution at the neck of a tension specimen, *Collected experimental papers* (1964). Harvard University Press.
- [8] M. A. Eisenberg, Anisotropic tensile necking, *International Journal of Plasticity* 1 (1985) 29–38.
- [9] J. P. Noble, B. D. Goldthorpe, P. Church, J. Harding, The use of the hopkinson bar to validate constitutive relations at high rates of strain, *Journal of the Mechanics and Physics of Solids* 47 (1999) 1187–1206.

- [10] H. Yang, X. Su, B. Bai, Analysis of diametral strain in uniaxial tensile and compression testing of round specimens of anisotropic materials, *International journal of mechanical sciences* 42 (2000) 2395–.
- [11] D. S. McDarmaid, A. W. Bowen, P. G. Partridge, Superplastic deformation of strongly textured ti-6 al-4 v, *Journal of Materials Science* 19 (1984) 2378–2386.
- [12] M. Rittenhouse, P. Picklesimer, Metallurgy of zircaloy-2. part ii. the effects of fabrication variables on the preferred orientation and anisotropy of strain behavior (1961).
- [13] M. R. Arthington, C. R. Siviour, N. Petrinic, B. C. F, Cross-section reconstruction during uniaxial loading, *Measurement Science and Technology* 20 (2009) 075701.
- [14] E. Wielewski, M. R. Arthington, C. R. Siviour, S. Carter, F. Hofmann, A. M. Korsunsky, N. Petrinic, A method for the in situ measurement of evolving elliptical cross-sections in initially cylindrical taylor impact specimens, *The Journal of Strain Analysis for Engineering Design* (2010).
- [15] U. F. Kocks, C. N. Tome, H. R. Wenk, *Texture and anisotropy: Preferred orientations in polycrystals and their effect on materials properties* (1998).
- [16] Astm e517-00(2006), standard test method for plastic strain ratio r for sheet metal, 2006.

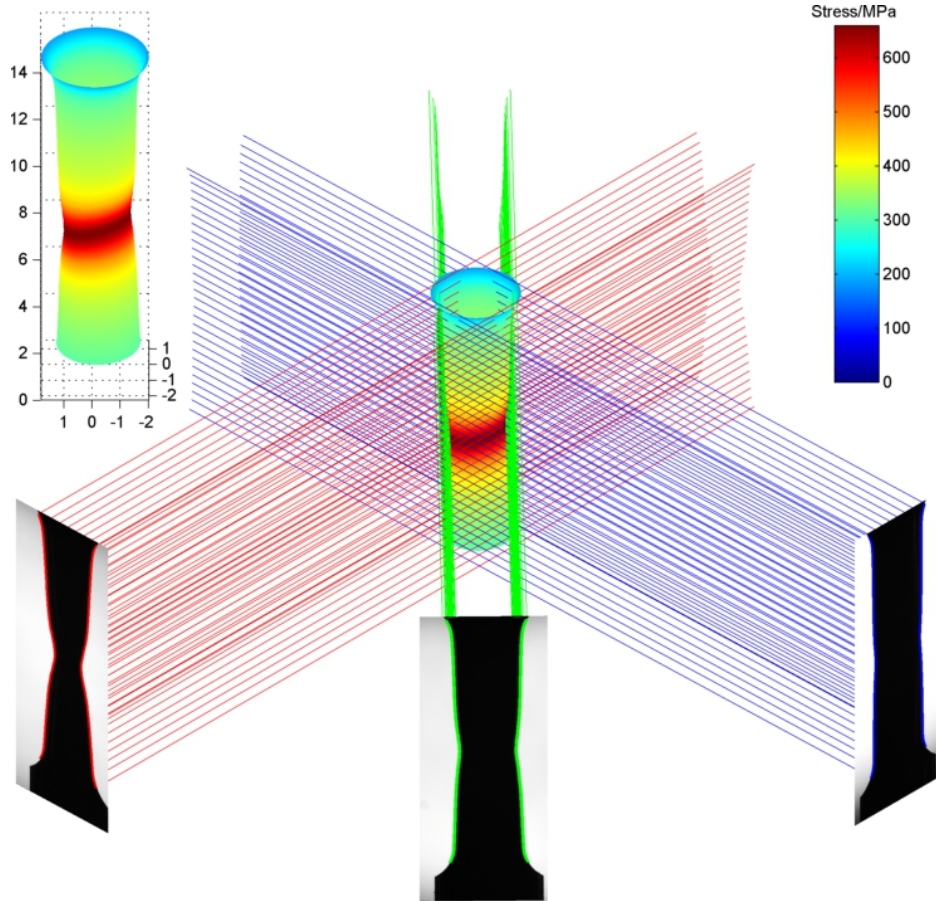


Figure 1: An overview of the optical technique used to estimate the elliptical shape of specimen cross-sections. For clarity, a coarser representation of the number of tangential edges found in the three camera views of the specimen is shown than that found obtained during analysis. The specimen shape is estimated within the space left by the lines, and is also shown inset on mm axes, and it is shaded according to the mean direct true stress.

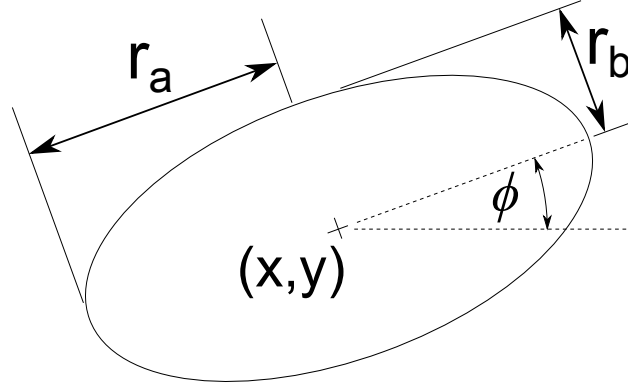


Figure 2: Definition of ellipse parameters.

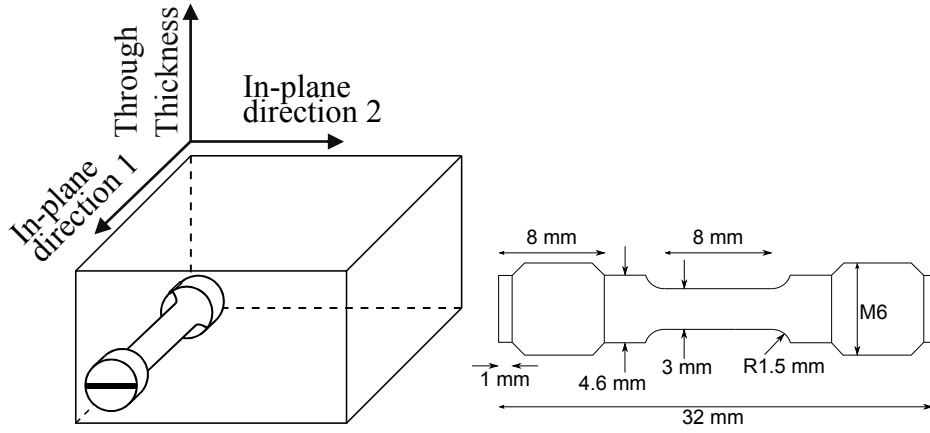


Figure 3: Schematic diagram of Zirconium specimen orientation in the parent plate, indicating identical in-plane directions and the through thickness direction. A score in the end of the specimen was used for alignment. Also shown are the nominal dimensions of the cylindrical dog-bone shape.

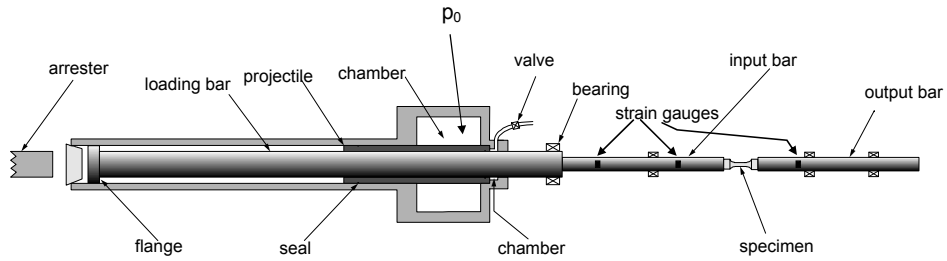


Figure 4: Schematic diagram of tensile split-Hopkinson bar.

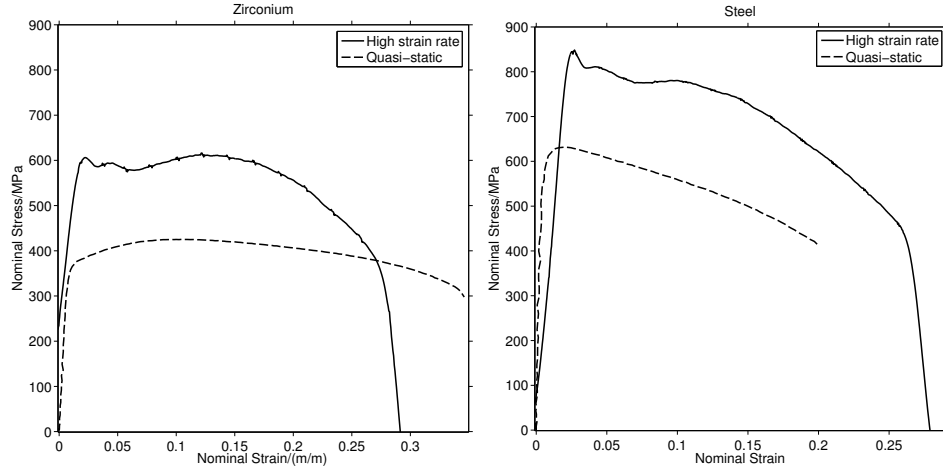


Figure 5: Nominal stress-strain curves.

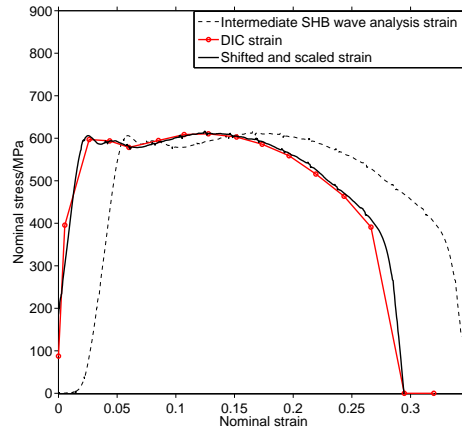


Figure 6: Calculation of nominal stress-strain curve in Zr from Hopkinson bar experiments using optical measurement of deformation.

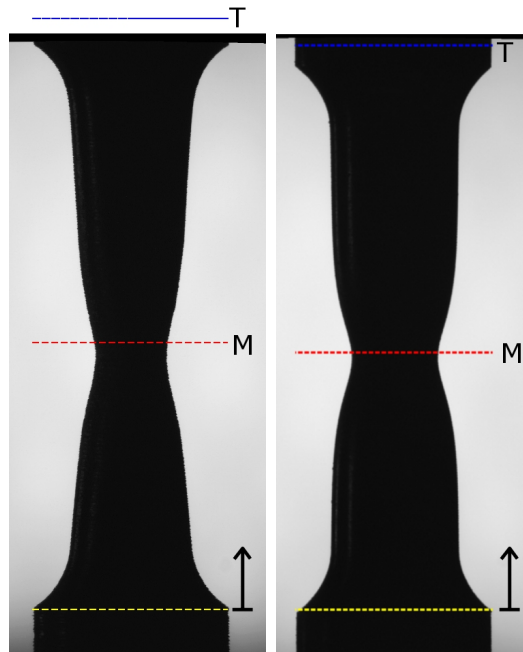


Figure 7: Images of interrupted quasi-static specimens before removal from the loading apparatus, showing the locations on the specimen where CMM data were obtained, M (middle) and T (top) lines, and the origin of the axial coordinates, the lower line. On the left is Zirconium viewing its narrowest diameter, on the right, Steel.

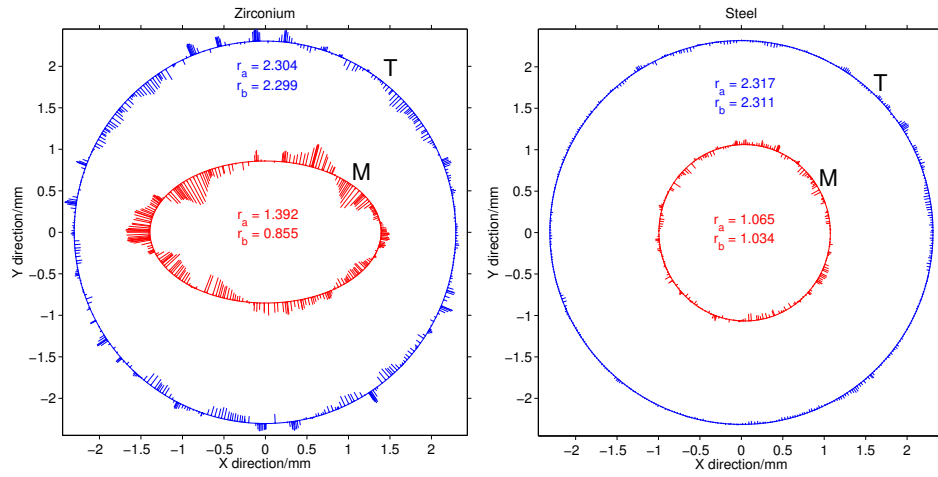


Figure 8: Ellipse fit to CMM co-ordinate data from two positions on the specimen surface, shown in figure 7. Error ‘spikes’ show the distance from each data point to the best fit ellipse. The spikes are shown 20 times larger than the actual error size. The two cross-sections shown were the worst-case fits inside and outside of the gauge section.

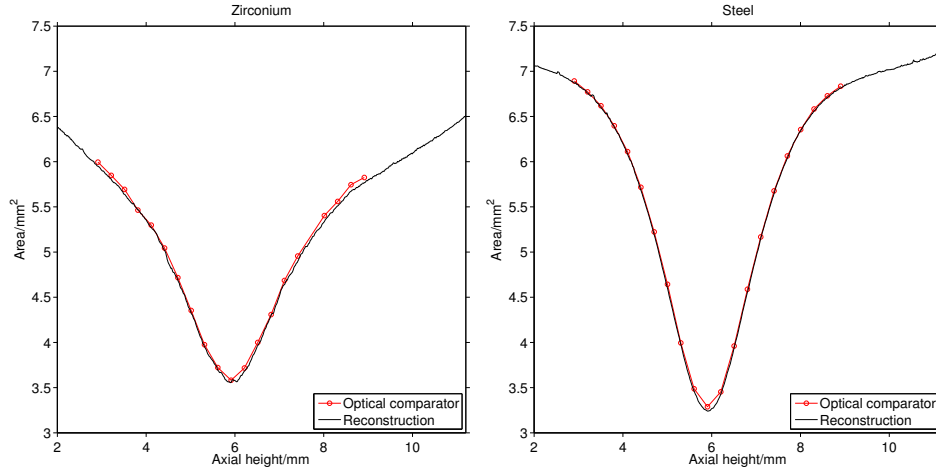


Figure 9: Comparison of specimen area as a function of axial position, from geometric reconstruction and optical comparator.

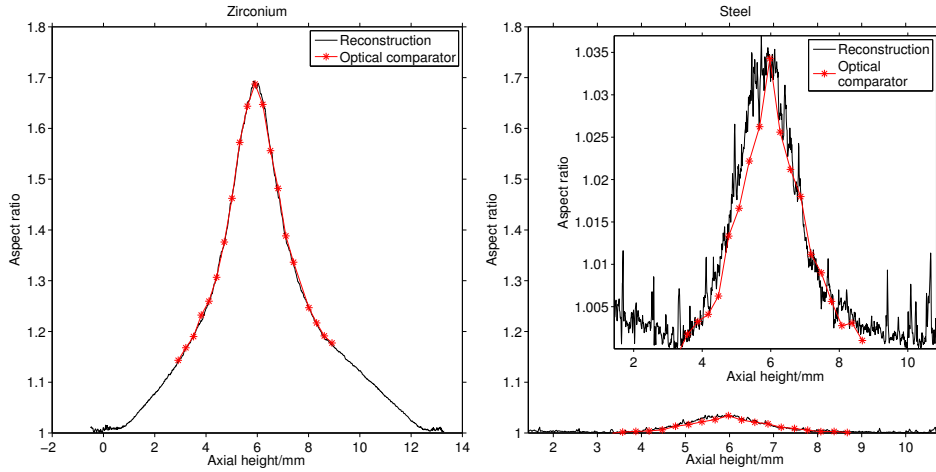


Figure 10: Comparison of aspect ratios calculated from geometric reconstruction and the interpolated optical comparator data, as a function of axial position. * indicate the axial positions of the optical comparator data. Data from the steel specimen are shown on the same scale as the Zirconium and, inset, on an enlarged scale.

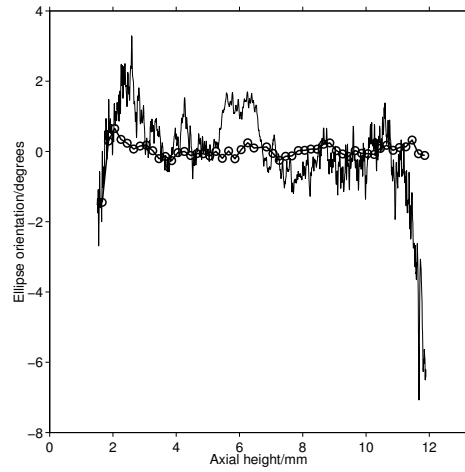


Figure 11: Orientation of the cross-section ellipses in the interrupted Zirconium specimen calculated by the geometric reconstruction and fitted to the CMM data, showing that the orientation is independent of axial position (and therefore strain). Circles indicate the position of CMM data.

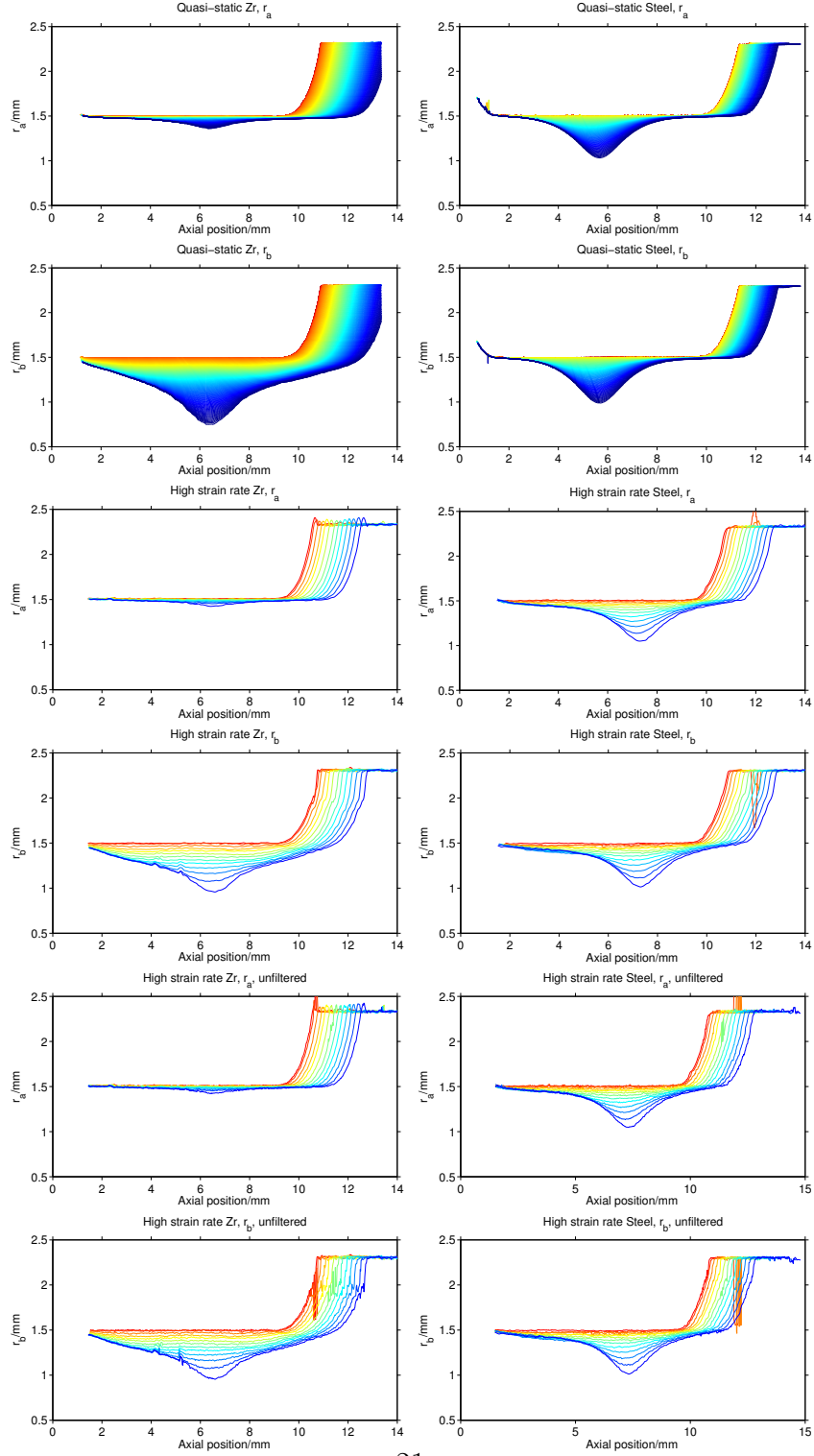


Figure 12: Semi-major and semi-minor axes calculated by the geometric reconstruction at quasi-static and high strain rates for both Zirconium and Steel. For the high rate data, both filtered (smoothed) and unfiltered versions are shown.

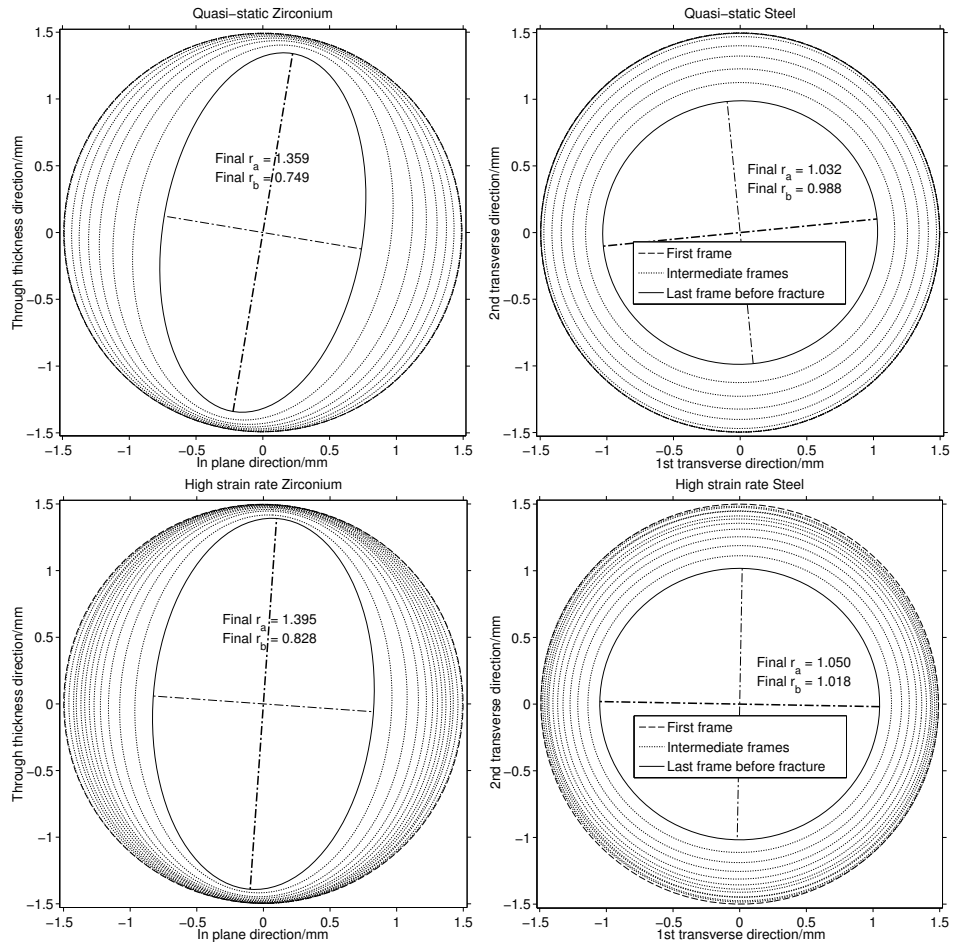


Figure 13: Reconstructed cross-sections from different stages of the deformation. For the high rate data, all frames are shown, whilst every 10th frame is shown for the quasi-static data, as well as the first and final frames of the experiment.

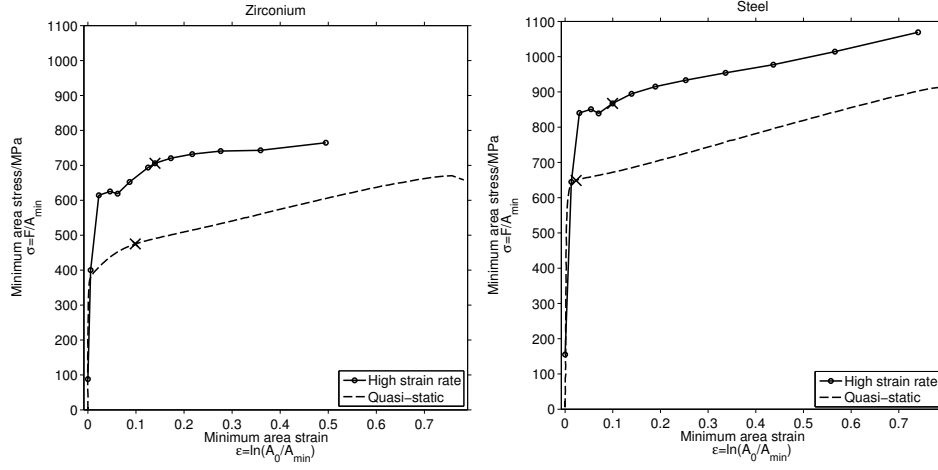


Figure 14: Mean true direct stress-strain curves produced using data from the geometric reconstruction. In each case, the area of the minimum cross-section is used to calculate mean stress and mean strain. Crosses indicate the position at which the Ultimate Tensile Strength (UTS) was recorded.

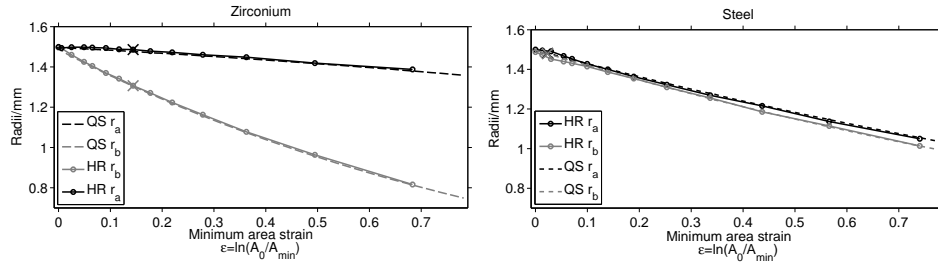


Figure 15: Semi-major and semi-minor axes as functions of axial strain. Data are from the minimum cross section of the specimen. Crosses indicate the position at which the Ultimate Tensile Strength (UTS) was recorded. QS = quasi-static. HR = high strain rate.

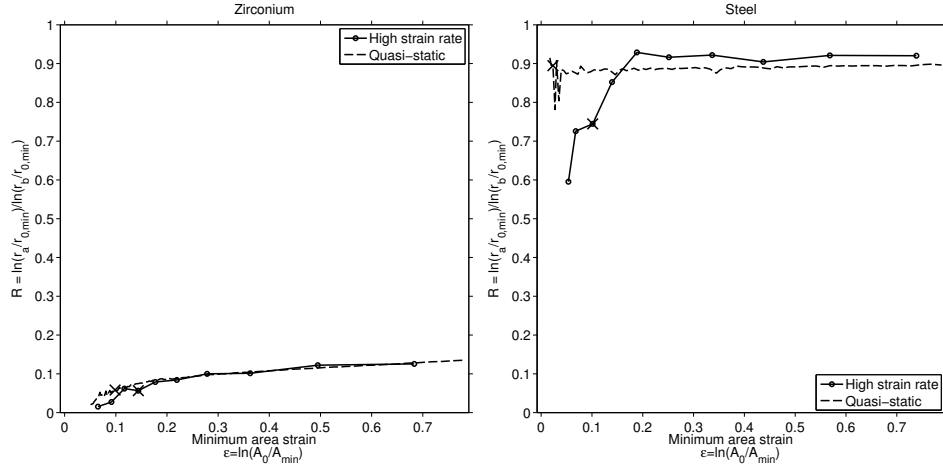


Figure 16: R ratio as a function of axial strain at the minimum cross section of the specimen. Crosses indicate the position at which the Ultimate Tensile Strength (UTS) was recorded.

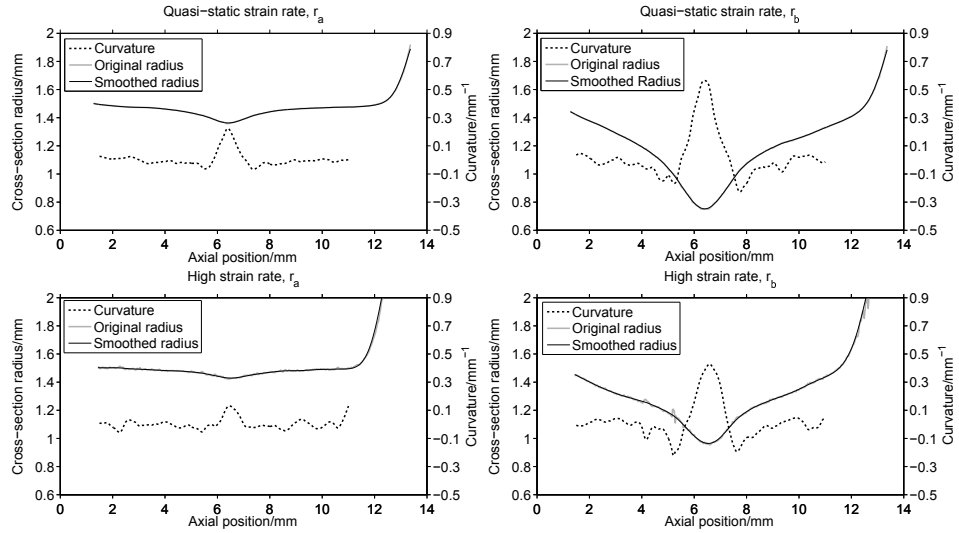


Figure 17: Radii and curvature calculated from low and high strain rate tensile Zirconium specimens, in both the major and minor axes.